Femtosecond Laser Induced Breakdown Spectroscopy of Cu at the micron/sub-micron scale

Vassilia Zorba,[a*] Xianglei Mao[a] and Richard E. Russo[a,b]

[a] *Lawrence Berkeley National Laboratory, Berkeley, CA 94720, USA.*
[b] *Applied Spectra, 46661 Fremont Blvd., Fremont, CA 94538, USA.*

While femtosecond Laser Induced Breakdown Spectroscopy has been studied in the macro-scale (i.e. ablation crater sizes of tens to hundreds of micrometers), the spectral emission mechanisms at the micron/sub-micron scale remain largely unknown, mainly because of the challenges associated with spectral emission acquisition from the limited amounts of ablated mass at these small lengthscales. In this work we study the limits of detection, the laser-induced plasma properties and spectral emission efficiency of Cu at the micron/submicron scale. Although the corresponding number electron densities and temperatures are similar to those reported for macroscale laser ablation, our findings suggest less efficient luminous spectral emission per ablated volume as we scale down in laser energy and crater sizes. These results provide a first insight into fs laser-induced plasma properties at the micron/sub-micron scale regime.

*Corresponding author e-mail: VZormpa@lbl.gov

1. Introduction

The advent of femtosecond (fs) lasers during the past decades offers a number of advantages in laser-material interactions. Non-linear absorption and non-thermal mechanisms lead to spatially (lateral) and axially (depth) confined laser-material interactions employing either near- and far-field laser ablation [1,2,3]. At sufficiently high laser energy density, the laser-material interaction results in plasma formation. Detection of the optical emission from the plasma, the basis of a technique known as Laser-Induced Breakdown Spectroscopy (LIBS), provides information on the chemical composition of the sample from which the plasma originated [4,5]. This technology offers surface (2D) and in-bulk (3D) elemental material analysis and chemical imaging capabilities [6,7].

One of the main objectives of laser ablation-based chemical analysis is control of the crater sampling area, which defines the spatial resolution. In any elemental analysis or elemental imaging application, the resolution has to be commensurate with the size of the smallest feature that is required to be chemically resolved. For many types of advanced material applications such as next generation energy related materials [8] (e.g. generation, conversion, storage), particle analysis, thin films and interfaces, etc., the resolution requirements usually range in the nanometer [9] to sub-micrometer scale. Conventional macro-scale LIBS crater sizes are several tens to hundreds of micrometers in diameter, therefore significantly limiting the use of this technique in these fields of applications.

Femtosecond lasers are widely used for high-precision ablation applications [4], including direct laser writing, 3D printing, cutting, functionalization etc. The differences in spatial and axial resolution that can be achieved with femtosecond as compared to nanosecond (ns) pulses, are traced back to the fundamentally different mechanisms of the laser-material interaction. The high non-linear absorption probability due to several orders of magnitude difference in peak intensity between fs- and ns- pulses, enables spatial and axial confinement of the femtosecond laser beam, which can under certain conditions, be smaller than the diffraction limit

[10]. Following laser absorption, the suppressed thermal effects associated with the concept of non-thermal ablation [11, 12], reduce signs of sample melting, resolidification and thermal load. All these effects are macroscopically manifested with well-defined craters (down to the hundreds of nanometers) with fs-pulses, and result in high precision laser ablation sampling as compared to ns-pulses [4].

Increasing the LIBS spatial resolution (reducing crater size), is associated with a concurrent reduction in the amount of ablated mass. However, for crater sizes smaller than ~0.5 μm, measurement of LIBS spectral emission becomes challenging using conventional emission monitoring in the far-field [3] and it is yet to be established whether emission exists with such small quantities of ablated mass.

Very few studies have addressed ablation at the few-micron/sub-micron scale, focusing on improving the absolute limits of detection with LIBS [2,3,13,14]. However, the fundamental plasma properties and their influence on the LIBS analytical behavior remain unknown. In this work we study the laser induced plasma properties and the resulting LIBS spectral emission characteristics of Cu in the few micron to submicron scale. We identify the limits of detection and spatial and axial resolution, as well as study plasma parameters (e.g. number density of electrons, excitation temperature) and spectral emission efficiency in the sub-micron scale. Finally, these plasma properties are compared to those reported for LIBS in Cu-based materials at the macro-scale. These findings provide insight into the mechanisms of LIBS spectral emission at small lengthscales, which are critical for improving spatial resolution for chemical analysis and imaging.

2. Experimental

A frequency doubled (400 nm) Ti:Sapphire laser (Mai-Tai oscillator TSA-25 amplifier, Spectra Physics) was used as the ablation source, delivering 100 fs pulses at a repetition rate of 1Hz. The sample used was a 99.999% pure Copper foil, (26,673-6, Sigma-Aldrich), with a thickness of 0.5 mm. A modified bright-field Olympus BX51 microscope system in reflection mode was used for

femtosecond laser beam delivery with submicron spot sizes (**Figure 1**). Laser irradiation was tightly focused on the Cu surface by a microscope objective lens (Nikon SLWD 50x, 0.45 Numerical Aperture). The focal spot size as defined by the numerical aperture of the microscope objective lens is 560nm (diffraction limit). The ablation process was monitored via a CMOS camera, through the same objective lens, to ensure that the surface always remained in focus. Due to the low depth of field of the microscope lens, any deviation within ~2 μm is evident through the imaging system and corrected for by moving the sample along the z-axis (**Figure 1**).

The light from the laser induced plasma was imaged onto a single fibre bundle, which was connected to the entrance slit of a spectrometer/ICCD camera system (HORIBA Jobin Yvon /Princeton Instruments). The gate of the ICCD camera was triggered by the laser and the relative delay was controlled by the camera. The focal length of the spectrometer was 460 mm with an f number of 5.3. The plasma was imaged on to a fibre bundle by using a UV fused silica plano-convex lens. All ablation craters were produced by using single laser pulse irradiation in ambient air. There were no observed matrix issues associated with sampling in air at the micron/sub-micron lengthscales. The laser pulse energy was measured with an Ophir PD10-PJ energy meter. Neutral density filters (CVI-NDQS) were used to attenuate the laser beam, and control the amount of energy that interacts with the sample surface. Following laser ablation, the samples were scanned by using a Nanoscope IV Atomic Force Microscope (AFM) in tapping mode to acquire the surface topographical image. Statistical analysis and line profiles of the surface features were obtained using the WSXM software.[15]

3. Results and Discussion

3.1 Limits of detection

Table 1 lists the three neutral Cu lines used in the LIBS experiments, along with their corresponding spectroscopic parameters. The strong atomic emission lines of Cu in the visible spectral range (510.55, 515.32 and 521.82 nm) are shown in

Figure 2(a)-(d) for decreasing laser energy**.** The AFM surface maps of the sampled Cu surfaces, together with their surface profiles are also shown for the different laser energies. The smallest crater size, defined as the full width at half maximum (FWHM) of the feature beneath the original surface, from which spectral emission could still be detected was 860 nm **(Figure 2(d))**. Under these conditions the ablated Cu mass was 1.4. 10^{-12} g, corresponding to 1.3 10^{10} ablated Cu atoms. Further details on the ablated crater metrics (FWHM, diameter, depth, volume) are given in *Section 3.3*.

Because of the transient nature of laser induced plasmas, the populations of the various species in the plume rapidly evolve with time and position [16]. The time resolved spectra and integrated emission intensity are shown in **Figure 3a** and **b** respectively, for a 5 ns gate width. For the first 10 ns after the laser pulse the spectral emission is characterized by an intense continuum background (**Figure 3a**). This emission is attributed to the Bremsstrahlung process, collisions of electrons with ions and atoms (free-free emission) and recombination of electrons with ions (free-bound emission).[17] At later times, the continuum emission intensity drops abruptly as a result of plasma expansion and cooling, and recombination processes to ground-state ions and excited atoms. The entire duration of spectral emission using the 2.53 μJ pulse was 70 ns, with the continuous emission taking place during the first 10 ns. In this case, the duration of the emission line is defined as the total time over which the emission signal intensity to noise ratio exceeds one. For lower energies, the emission persists around 20 to 30 ns. These emission times are orders of magnitude less than those measured using macro-scale laser ablation, where emission persistence typically range from several to tens of microseconds using ns and fs laser ablation of Cu and Cu-based alloys [18,19, 20, 21, 22].

3.2 Plasma Properties: Electron number density (n_e) and excitation temperature (T_e)

The three main parameters that influence spectral emission in a laser plasma are the number density of the emitting species, the electron number density (n_e) and the excitation temperature (T_e). The number density of the emitting species is a function of the total ablated mass, the excitation temperature and the degree of the excitation and/or ionization of the plasma [17]. For fs-induced plasmas where there is an absence of plasma shielding because of the short pulse duration, the ablated mass depends on the absorption of the laser irradiation defined by the optical properties of the sample, the sample thermal and physical properties, and the laser fluence.

The electron number density of a laser-induced plasma can be determined from the spectral line profile. The width of each spectral line is affected by broadening mechanisms which originate from the environment of the radiating atoms and ions. Predominant spectral line broadening mechanisms in laser plasmas are natural, Stark, Doppler, self-absorption and instrumental broadening [23,24]. In the experimental conditions of this work, the main mechanism contributing to spectral line broadening is the Stark effect. The FWHM of Stark broadened lines ($\Delta\lambda_{1/2}$) scales with the electron number density n_e. as:

$$\Delta\lambda_{1/2} = 2w\left(\frac{n_e}{10^{16}}\right) \quad (1)$$

where w is the electron width parameter. The temperature dependent values of w for the 521.8 nm line were taken from [25]. Lorentzian curve fitting of the experimental data was used to quantify the FWHM of each line. The resulting number electron density of the laser generated Cu plasma with time is given in **Figure 4a** (blue symbols). As shown here, the electron number density decays from 1.1 10^{17} to 1.1 10^{16}/cm^3 within the 70 ns duration of the laser plasma, for the highest laser energy conditions implemented. Under these conditions, the electron number density was found to decay with a dependence $n_e \propto t^{-1}$ rather than the $n_e \propto t^{-3}$ approximation of adiabatic expansion [26]. The electron number density integrated over 100 ns, a time which exceeds the emission persistence time, is shown in **Figure 4b** as a function of laser energy. The range of electron densities measured for micron/sub-micron scale LIBS as shown in **Figures 4a** and **4b** is in

agreement with densities reported in macro-scale ns laser ablation of Cu (order of 10^{16}cm^{-3}) [31,32].

One of the criteria used to define plasma properties is whether the system is in Local Thermodynamic Equilibrium (LTE). Determination of the electron number density using Stark-broadening does not require LTE, which assumes that the population and depopulation of atomic and ionic states occurs predominantly by collisions rather than by radiation. This collision process requires electron number density to be high enough to ensure high collision rates [27]. The lower limit of electron density required for LTE is given by the McWhirter criterion, which is a necessary, but not sufficient, criterion for LTE [28]:

$$n_e \geq 1.6 \times 10^{12}\, T^{\frac{1}{2}}\, \Delta E^3 \qquad (2)$$

Here T (K) is the excitation temperature and ΔE (eV) is the energy difference between the states that are expected to be in LTE. From **Equation 2** the lowest limit for n_e is 2 x 10^{15} cm^{-3} for the 521.82 nm transition. While the McWhirter criterion may be fulfilled at sufficient at sufficient delay after the laser pulse, it is not sufficient to verify LTE due to the inhomogeneous and transient nature of the LIBS plasma,, and results must be therefore carefully considered [29, 30].

The plasma excitation temperature can be determined using the Boltzmann plot method. The excitation temperature (T) as a function of the spectral line intensity I_{ki} is given by:

$$-\ln\left(\frac{\lambda_{ki} \cdot I_{ki}}{g_k \cdot A_{ki}}\right) = \frac{E_k}{T} + \ln\left(\frac{4 \cdot \pi \cdot Z(T)}{h \cdot c \cdot N}\right) \qquad (3)$$

where λ_{ki} and A_{ki} are the wavelength and probability of the transition $k \rightarrow i$, g_k and E_k the degeneracy and energy of the upper level k, N is the total number density of a species in a given ionization stage, T the excitation temperature and $Z(T)$ the partition function of Cu I. The plasma excitation temperature was derived for the atomic copper lines 510.55 nm, 515.32 nm and 521.82 nm using the spectroscopic parameters listed in **Table 1**.

The evolution of the excitation temperature with time after the laser pulse is shown in **Figure 4a** (black symbols). Similarly, the dependence of temperature on laser energy is shown in **Figure 4b**. As shown in **Figures 4a** and **4b,** excitation temperatures as high as 9500 K are observed in micon/sub-micron laser ablation of Cu, in agreement with temperatures observed in macro-scale LIBS [31,32], which for ns laser pulse irradiation, range from 8000 K to 12000 K. Similar to the trend shown for the electron number density, the temperature decay exhibits a deviation from adiabatic expansion with a decay proportional to $t^{-0.27}$. Similar decays have been reported in macro-scale (crater diameter of 150 μm) fs laser ablation of brass at 248 nm [21]. Nevertheless, faster decay rates have been found for 200 μm crater sizes, where a 527 nm fs laser was used as the irradiation source [19, 33].

3.3 Spectral emission efficiency

The crater volume, FWHM, lateral diameter, and average crater depth, are shown in **Figure 5a,** as a function of laser energy. The FWHM ranged from 0.86 to 1.56 μm with the lateral diameter varying from 1.4 to 3.2 μm; crater depth ranged from 250-800 nm. The ablation crater volume as a function of laser energy is shown in **Figure 5a. Figure 5b** depicts the integrated spectral emission normalized over the crater volume, plotted against laser energy. The ratio varies over two orders of magnitude with laser energy, indicating the existence of different spectral emission efficiencies across this laser energy range. The spectral emission from larger ablated craters appears to be more efficient compared to smaller craters. Although crater volume is associated with the amount of ablated mass, this mass does not necessarily contribute to LIBS spectral emission and could contribute to the change in the LIBS emission efficiency at small scales. Other factors that may contribute to this behavior may be the energy allocation (coupling), the part of the plasma that is imaged and plasma temperature distribution. The contribution of these factors is discussed in the next section.

3.3.1 Influence of Nanoparticles

Large concentrations of nanoparticles are known to exist in fs-laser induced plasmas at

the macroscale [34,35]. Our previous work using UV fs-ns double-pulse LIBS of Si demonstrated that non-radiative species/particles are present in the plasma and remain there long after the luminous emission has ended [36]. Therefore, at these small-lengthscales, only a portion of the ablated material leads to LIBS emission, whereas the rest is in the form or non-emitting particles. Since the excitation temperature is nearly independent of laser energy input (**Figure 3b**), the differences in emission efficiency may be attributed to an increasing concentration of non-emitting nano particles vs. emitting species as we scale down in laser energy and crater sizes.

3.3.2 Laser energy coupling

In any laser-material interaction, the pulsed laser energy absorbed by any sample is distributed towards plasma formation, material removal, as well as to melting and hydrodynamic redistribution of molten mass. This process may lead to liquid material redistribution towards the periphery of the ablation craters, often resulting in the formation of rims that protrude above the material surface. Even though this phenomenon is much more pronounced using nanosecond laser ablation, similar effects can be observed in femtosecond laser ablation due to non-thermal melting. In the experimental conditions of this work the size of the rims is small compared to the craters, (crater profiles in **Figure 2)** and as a result, the relative contribution of non-thermal melting is not expected to be substantial or affect the LIBS emission efficiency as a function of energy.

3.3.3 Plasma Imaging

Control over the plasma imaging conditions in any LIBS experiment is important to ensure reliable and reproducible analytical results. Ideally the entire expanding plasma should be imaged onto the light collection optics, to ensure that information from the entire ablation event is recorded in a LIBS spectrum. In many cases for macro-scale ablation, because of the size and duration of the plasma, only a portion of the plasma is measured. However, in the case of small plasmas (maximal crater volume of ~2 μm^3-**Fig.5a**) with short emission persistence times

(<70 ns), spectral emission from the entire expanding plasma is expected to be recorded, based on the collection optics used. As a result, no contribution from partial plasma imaging on the LIBS efficiency results is anticipated.

3.3.4 Temperature Distribution

For the laser energy range used in this work, we find that even though the crater volume decreased significantly **(Figure 5a**), the temporally-integrated excitation temperature did not change drastically (**Figure 4b)**. However, apart from the absolute excitation temperature values, the distribution of the excitation temperature also can affect the spectral emission efficiency. Because of the transient nature of the laser plasma, the distribution of the excitation temperature is spatially inhomogeneous (e.g. **Figure 6a)**. As a result, the excitation temperatures calculated from the experimental data have significant contributions from the hotter areas and do not sufficiently represent the true spatially integrated mean excitation temperature (T_{mean}). For that reason a numerical simulation was incorporated to establish a better understanding of the true excitation temperature and its distribution.

We treat the plasma as a 3-dimensional expanding hemisphere, starting from r=0 to r=R, where *R* is the maximal plasma radius (**Figure 6a**) and *a* is a variable. The following boundary conditions were satisfied: the maximum temperature occurs for r=0, and a zero temperature for r=R. The hyperbolic function that satisfies these conditions is:

$$T(r) = -To \cdot \frac{r-R}{ar+R} \qquad (4)$$

After establishing the temporal distribution for different *a* values (solid lines in **Figure 6b**), we combined the spectral line intensity equation, the Saha-Boltzman equilibrium and the mass conservation equation and adopted the Boltzmann Plot Method, to numerically solve for temperature T_{model} (open symbols in **Figure 6b**). The mean temperature T_{mean} (full symbols) also is calculated for each distribution (different *a* values). In all cases T_{mean} is significantly lower than the model predicted temperature (T_{model}) indicating that the excitation temperature in the laser

plasma is overestimated. The difference between the two temperatures becomes larger for a=10 which corresponds to the steepest, most abrupt temperature decay.

Based on these findings, the experimentally measured excitation temperature for different a model distribution values, is overestimated as compared to mean temperature. Furthermore, the way in which the ratio between the two temperatures changes, is non-linear. Different laser energies may account for different distributions. As a result, the excitation temperatures that we measure experimentally using conventional methods (**Figure 4b**) may not be representative, and the true mean temperature can in fact change as a function of energy. A change in the mean excitation temperature (T_{model}) with laser energy is consistent with the different emission efficiencies we observe for Cu in the micron/submicron scale (**Figure 5b**).

Further work on direct fs-laser induced plasma imaging is underway to better understand the observed emission behavior, and correlate ablation efficiency to plasma properties and nanoparticle generation, as they relate to LIBS analytical performance in the sub-micron scale.

4. Summary

We studied the micron/sub-micron scale LIBS spectral emission characteristics and the plasma properties for Cu. The absolute limits of detection, spatial and axial resolution, and spectral emission properties were studied. The number density of electrons and temperature in this plasma were similar with those reported in macro-scale LIBS. Despite these similarities, our results demonstrate significantly reduced spectral emission efficiency (emission intensity over sampled material volume) as we scale down in energy. These results provide a first insight in the inherent plasma properties and mechanisms of LIBS spectral emission at small lengthscales.

Acknowledgements

This research has been supported by Laboratory Directed Research and Development (LDRD) funding from Berkeley Lab, provided by the Director, Office of Science, of the U.S. Department of Energy. This work also was supported by the Chemical Science Division, Office of Basic Energy Sciences, and the U.S. Department of Energy under Contract No.DE-AC02-05CH11231.

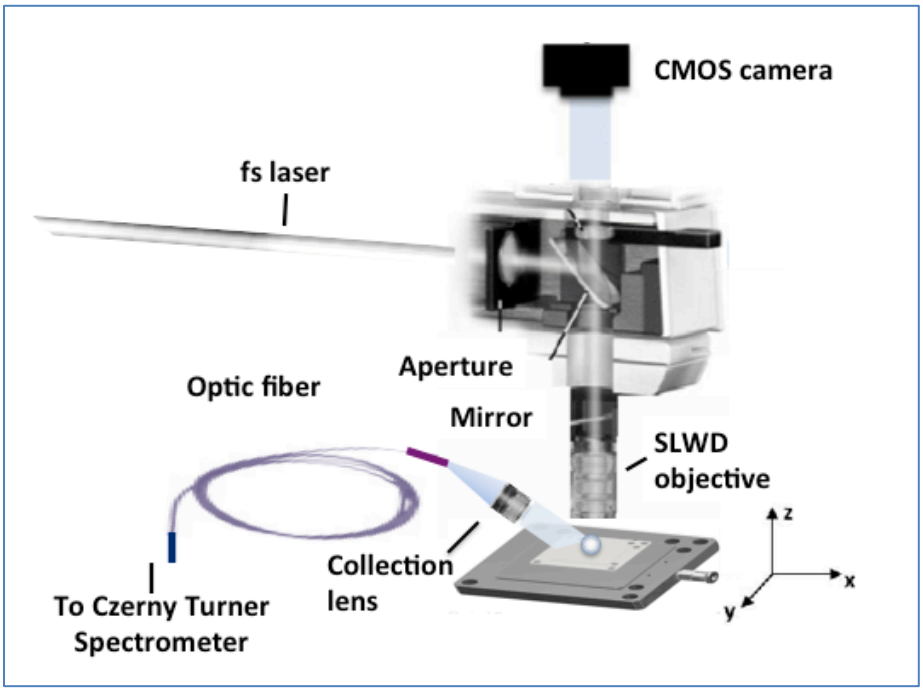

Figure 1: Schematic of the sub-micron LIBS experimental setup.

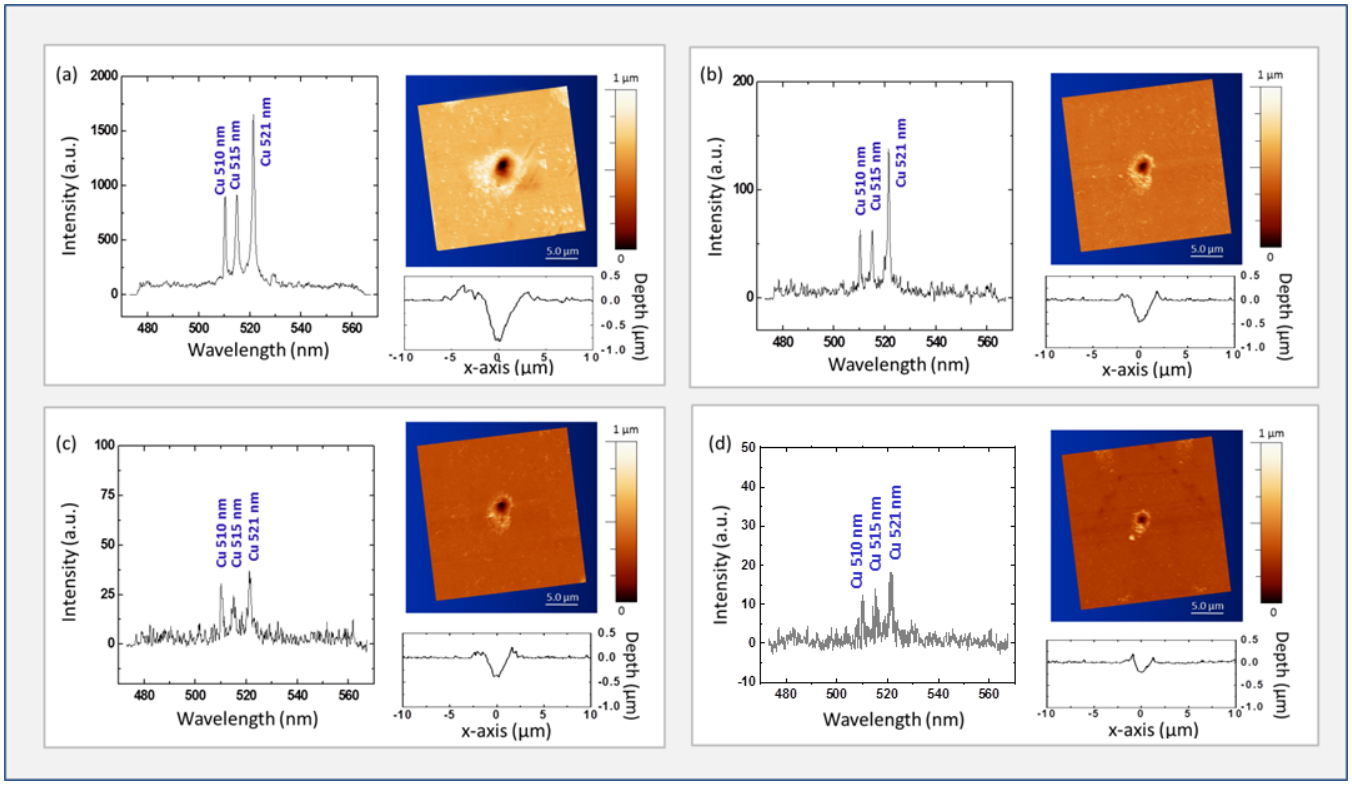

Figure 2: Cu I LIBS spectral emission, AFM surface maps of the corresponding craters and their surface profiles, generated by a single 400 nm, 100 fs laser pulse at **(a)** 2.53 µJ, **(b)** 250 nJ, **(c)** 160 nJ and **(d)** 100 nJ. The LIBS emission fluence threshold (d) was 5J/cm^2. The ICCD integration time was 100 ns.

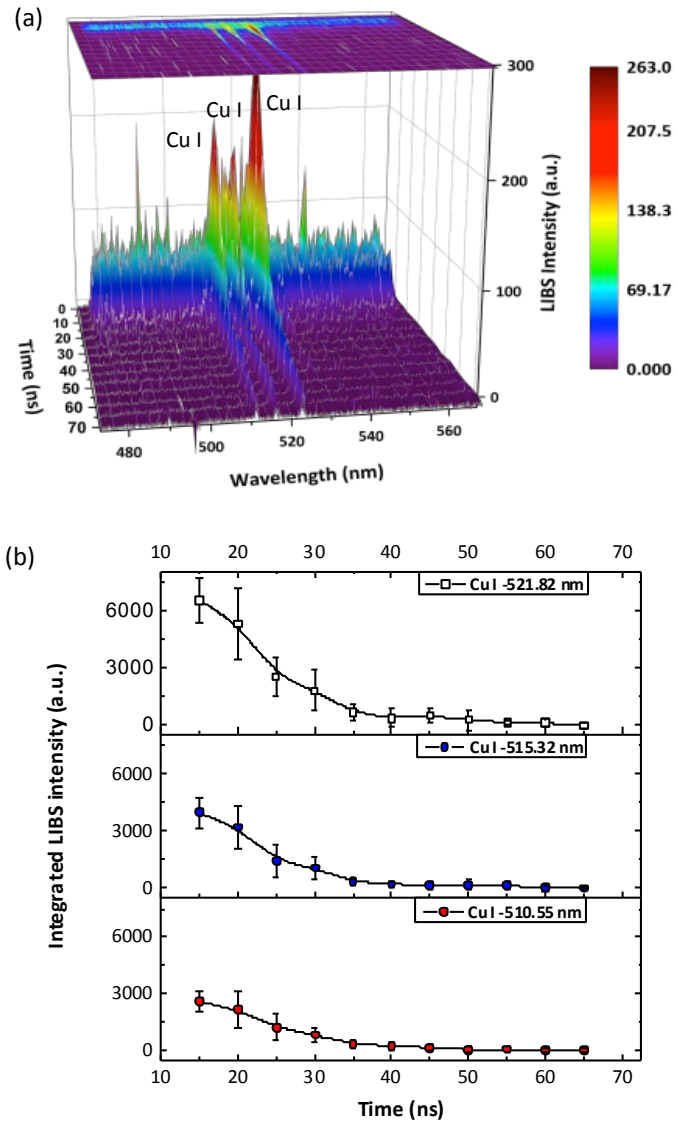

Figure 3: (a) Time resolved LIBS spectral emission at 2.53 μJ, and **(b)** integrated emission intensity of the Cu I lines at the same energy, as a function of time after the laser pulse. The sampling gate width was 5 ns. Integrated LIBS intensity could not be accurately measured during the first 10 ns due to the poor signal-to-noise ratio from continuum emission.

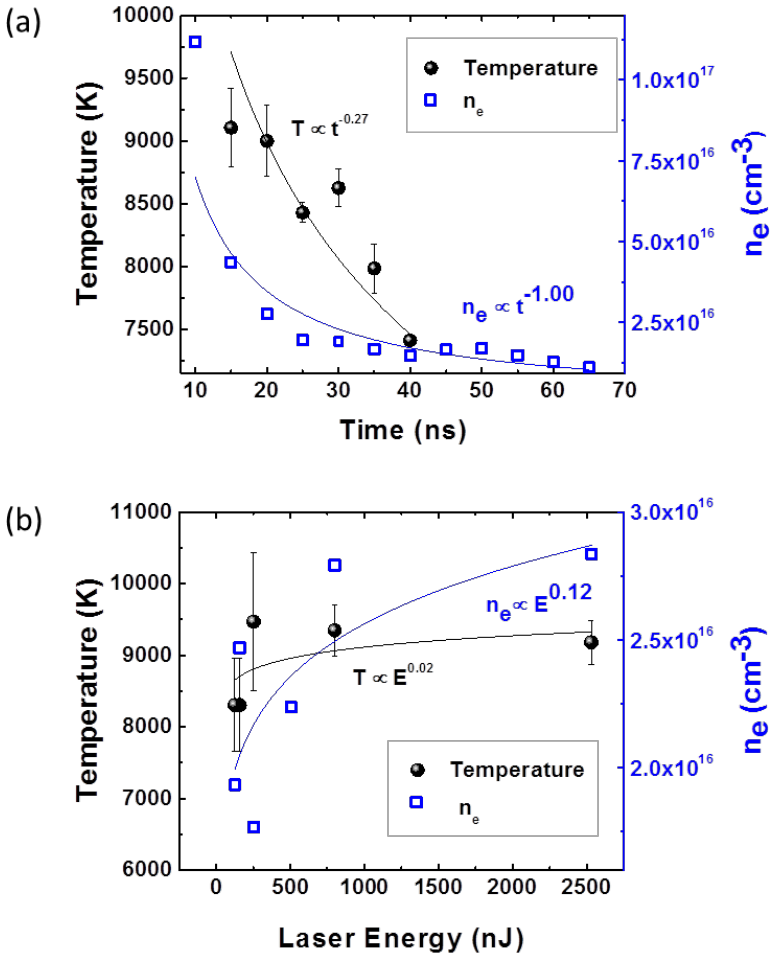

Figure 4: (a) Time resolved excitation temperature (black symbols) and number density of electrons (blue symbols) for 2.53 μJ incident laser energy. A t^{-b} type function was used to fit the experimental data (solid lines). The ICCD integration step was 5 ns. **(b)** Calculated excitation temperatures (black) and number density of electrons (blue) as a function of laser energy. The ICCD gate width was 100 ns. An E^c type function was used to fit the experimental data.

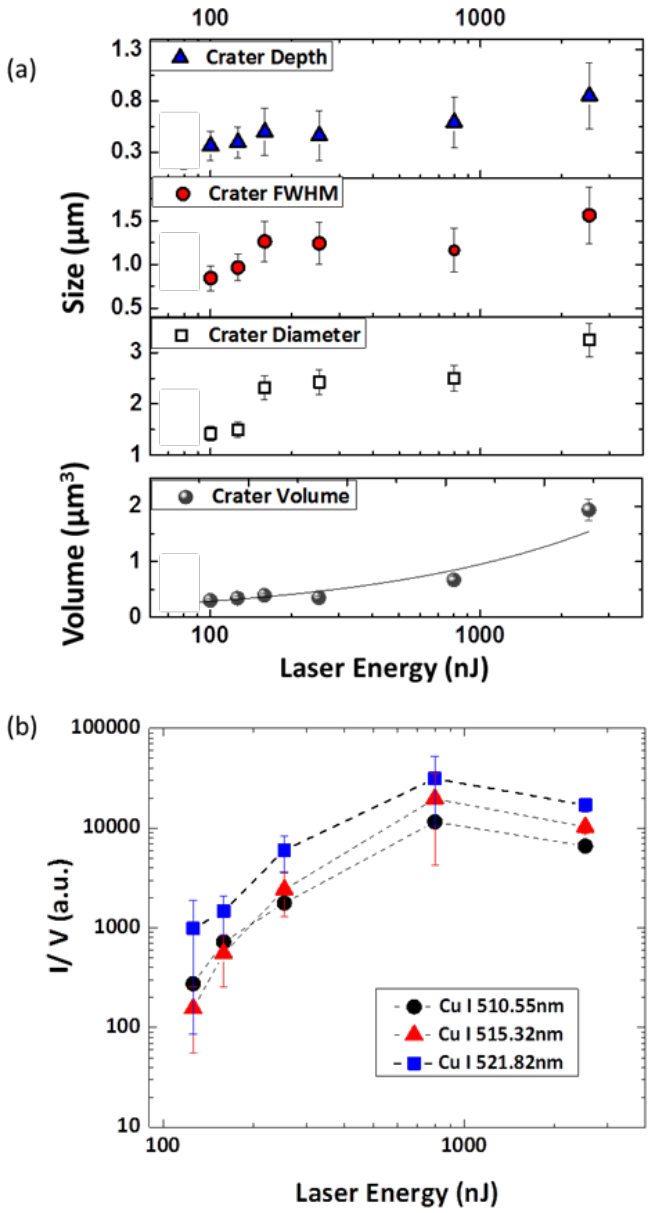

Figure 5: (a) The crater size (Full diameter, FWHM, crater depth and volume as a function of laser energy. The line is a fit of the crater volume data to the square root of laser energy. **(b)** The integrated emission intensity normalized over crater volume as a function of laser energy, for the three different atomic copper lines.

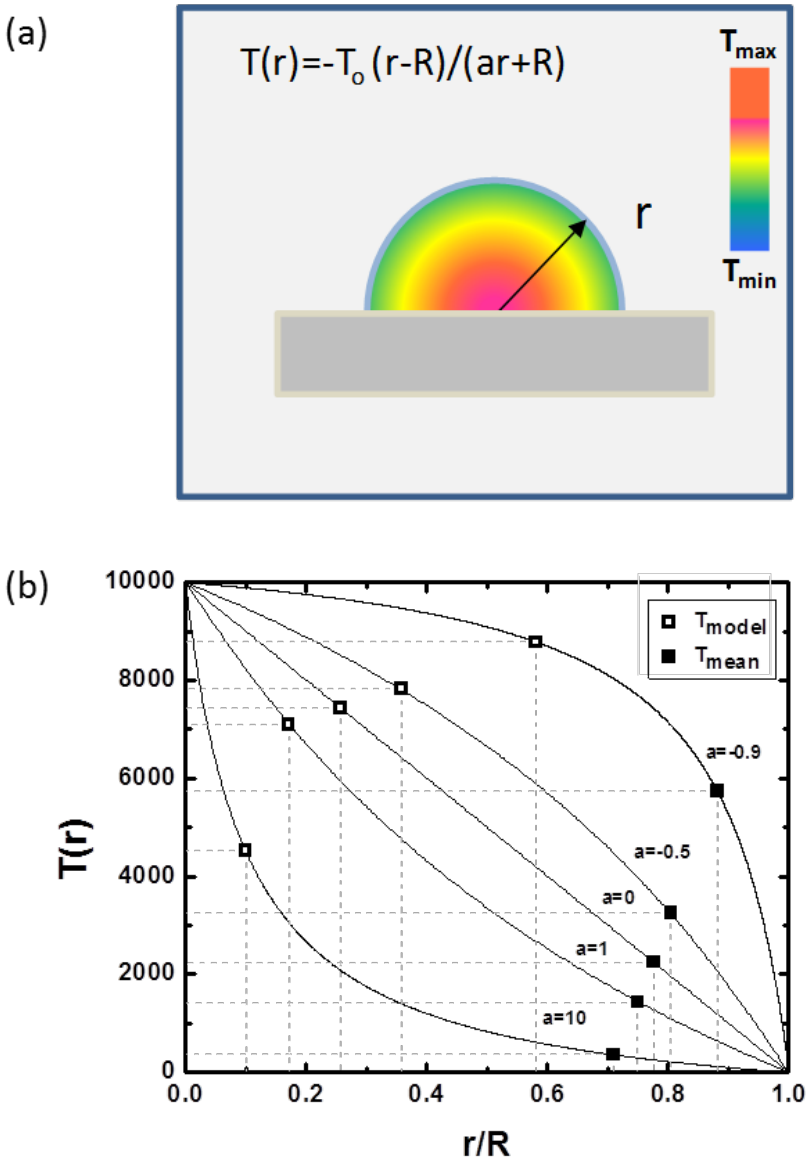

Figure 6: (a) Model of temperature distribution and (b) corresponding excitation temperature distribution for different *a* values based on a 3-D expanding hemispheric plasma. The model calculates the temperature corresponding to the numerical solution of the model (T_{model}) is shown in open symbols. The mean temperature for each one of different *a* values shown in full symbols (T_{mean}).

Table 1. List of Cu lines and corresponding spectroscopic parameters.

λ/nm	**E_k/eV**	**E_i/eV**	**Configuration**	**A_{ki}/s^{-1}**	**g_k**	**g_i**
510.55	3.817	1.389	$3d^9 4s^2$ - $3d^{10}(^1S)4p$	2.0E+06	4	6
515.32	6.191	3.786	$3d^{10}(^1S)4p$ - $3d^{10}(^1S)4d$	6.0E+07	4	2
521.82	6.192	3.817	$3d^{10}(^1S)4p$ - $3d^{10}(^1S)4d$	7.5E+07	6	4

Table I: Transition wavelength (λ), upper (E_k) and lower (E_i) energy levels, upper (g_k) and lower (g_i) level statistical weights and transition probability (A_{ki}) for the Cu I emission lines. Data reproduced from [37, 38].

References

[1] V. Zorba, X. Mao, R.E. Russo, Laser wavelength effects in ultrafast near-field laser nanostructuring of Si, Appl. Phys. Lett. 95 (2009) 041110-1-3.

[2] V. Zorba, X. Mao, R.E. Russo, Optical far-and near-field femtosecond laser ablation of Si for nanoscale chemical analysis, Anal. Bioanal. Chem. 396 (2010) 173-180.

[3] V. Zorba, X. Mao, R.E. Russo, Ultrafast Laser Induced Breakdown Spectroscopy for high spatial resolution chemical analysis, Spectrochim. Acta B 66 (2011) 189-192.

[4] D. Bäuerle Laser Processing and Chemistry; Springer: Berlin 2000.

[5] R.E. Russo, T.W. Suen, A.A. Bol'shakov, J. Yoo, O. Sorkhabi, X.L. Mao, J.J. Gonzalez, D. Oropeza, and V. Zorba. Laser Plasma Spectrochemistry J. Anal. At. Spectrom. 26 (2011) 1596.

[6] G. Nicolas, M. P. Mateo and V. Piñon, 3D chemical maps of non-flat surfaces by laser-induced breakdown spectroscopy, J. Anal. At. Spectrom. 22 (2007) 1244.

[7] J.R. Chirinos, D.D. Oropeza, J.J. Gonzalez, H. Hou, M. Morey, V. Zorba and R.E. Russo, 2014, Simultaneous 3-dimensional elemental imaging with LIBS and LA-ICP-MS, J. Anal. At. Spectrom. 29 (2014) 1292-1298.

[8] H. Hou, L. Cheng, T. Richardson, G. Chen, M. Doeff, R. Zheng, R. Russo, V. Zorba, Three-dimensional elemental imaging of Li-ion solid-state electrolytes using fs-laser induced breakdown spectroscopy (LIBS), J. Anal. At. Spectrom. (2015) DOI: 10.1039/C5JA00250H

[9] V. Zorba, J. Sysdek, X. Mao, R.E. Russo and R. Kostecki, Ultrafast laser induced breakdown spectroscopy of electrode/electrolyte interfaces, Appl. Phys. Lett. (2012) 100, 234101.

[10] F. Korte, J. Serbin, J. Koch, A. Egbert, C. Fallnich, A. Ostendorf, B. Chichkov, Towards nanostructuring with femtosecond laser pulses, Appl. Phys. A 77, (2003) 229–235.

[11] D. von der Linde , K. Sokolowski-Tinten, J. Bialkowski, Laser–solid interaction in the femtosecond time regime, Appl. Surf. Sci. 109 (1997) 1–10.

[12] D. von der Linde), K. Sokolowski-Tinten, The physical mechanisms of short-pulse laser ablation, Appl. Surf. Sci.154–155 (2000) 1–10.

[13] A. Assion, M. Wollenhaupt, L. Haag, F. Mayorov, C. Sarpe-Tudoran, M. Winter, U. Kutschera and T. Baumer, Femtosecond laser-induced-breakdown spectrometry for Ca2+ analysis of biological samples with high spatial resolution, Appl. Phys. B 77, (2003) 391-397.

[14] D.J. Hwang, H. Jeon, C.P. Grigoropoulos, J. Yoo and R.E. Russo, Femtosecond laser ablation induced plasma characteristics from submicron craters in thin metal film, Appl. Phys. Lett. 91 (2007) 251118-1-251118-3.

[15] I. Horcas, R. Fernandez, J. M. Gomez-Rodriguez, J. Colchero, J. Gomez-Herrero, and A. M. Baro, WSXM: A software for scanning probe microscopy and a tool for nanotechnology, Rev. Sci. Instruments 78 (2007) 013705-1-013705-8.

[16] B. Le Drogoff, J. Margot, M. Chaker, M. Sabsabi, O. Barthelemy, T.W. Johnston, S. Laville, F. Vidal, and Y. von Kaenel, Temporal characterization of femtosecond laser pulses induced plasma for spectrochemical analysis of aluminum alloys, Spectrochim. Acta B 56 (2001) 987-1002.

[17] A. Elhassan, A. Giakoumaki, D. Anglos, G. M. Ingo, L. Robbiola, M. A. Harith, Nanosecond and femtosecond Laser Induced Breakdown Spectroscopic analysis of bronze alloys. Spectrochimica Acta Part B-Atomic Spectroscopy 2008, 63. 504-511.

[18] Y. Li, C.H. Hu, H.Z. Zhang, Z.K. Jiang, and Z.S. Li, Optical emission enhancement of laser-produced copper plasma under a steady magnetic field. Applied Optics 48 (2009) B105-B110

[19] A. Santagata, A. De Bonis, P. Villani, R. Teghil, G. P. Parisi, Fs/ns-dual-pulse orthogonal geometry plasma plume reheating for copper-based-alloys analysis. Appl. Surf. Sci. 252 (2006) 4685-4690.

[20] L. Caneve, F. Colao, R. Fantoni, V. Spizzichino, Laser ablation of copper based alloys by single and double pulse laser induced breakdown spectroscopy. Appl. Phys. A 86 (2006) 151-157.

[21] V. Pinon, D. Anglos, Optical emission studies of plasma induced by single and double femtosecond laser pulses. Spectrochim. Acta B 64 (2009) 950-960.

[22] A. Elhassan, A. Giakoumaki, D. AngloS, G. M. Ingo, L. Robbiola, M. A. Harith, Nanosecond and femtosecond Laser Induced Breakdown Spectroscopic analysis of bronze alloys. Spectrochim. Acta B 63 (2008) 504-511.

[23] B.Y. Man, Q.L. Dong, A.H. Liu, X.Q. Wei, Q.G. Zhang, J.L. He, X.T. Wang, Line-broadening analysis of plasma emission produced by laser ablation of metal Cu, J. Opt. 6 (2004) 17-21.

[24] H.R Griem (Ed.), Plasma Spectroscopy, McGraw Hill, New York, 1964.

[25] N. Konjevic, W.L. Wiese, Experimental Stark widths and shifts for spectral lines of neutral and ionized atoms (A critical review of selected data for the period 1983 through 1988), J. Phys. Chem. Ref. Data 19 (1990) 1307-1385.

[26] P.T. Rumsby, and J.W.M. Paul, Temperature and density of an expanding laser produced plasma, Plasma Phys. Contr. F. 16 (1974) 247-260.

[27] B. Le Drogoff, J. Margot, M. Chaker, M. Sabsabi, O. Barthelemy, T.W. Johnston, S. Laville, F. Vidal, and Y. von Kaenel, Temporal characterization of femtosecond laser pulses induced plasma for spectrochemical analysis of aluminum alloys, Spectrochim. Acta B 56 (2001) 987-1002.

[28] D. W. Hahn, N. Omenetto, Laser-Induced Breakdown Spectroscopy (LIBS), Part I: Review of Basic Diagnostics and Plasma-Particle Interactions: Still-Challenging Issues Within the Analytical Plasma Community. Appl. Spectrosc. 64 (2010) 335A-366A.

[29] J.R. Freeman, S.S. Harilal , P.K. Diwakar , B. Verhoff , A. Hassanein, Comparison of optical emission from nanosecond and femtosecond laser produced plasma in atmosphere and vacuum conditions. Spectrochim. Acta B 87 (2013) 43–50.

[30] G. Cristoforetti, A. De Giacomo, M. Dell'Aglio, S. Legnaioli, E. Tognoni, V. Palleschi, N. Omenetto, Local Thermodynamic Equilibrium in Laser-Induced Breakdown Spectroscopy: Beyond the McWhirter criterion. Spectrochim. Acta B 65 (2010), 86–95.

[31] M A Hafez, M A Khedr, F F Elaksher, Y E Gamal, Characteristics of Cu plasma produced by a laser interaction with a solid target, Plasma Sources Sci. Technol. 12 (2003) 185-198.

[32] B. Rashid, S. Hafeez, N.M. Shaikh, M. Saleem, R. Ali, and M.A. Baig, Diagnostics of copper plasma produced by the fundamental, second and third harmonics of a Nd : YAG laser. Int. J. Mod Phys B 21 (2007) 2697-2710.

[33] A. Santagata, R. Teghil, G. Albano, D. Spera, P. Villani, A. De Bonis, G. P. Parisi, A. Galasso, fs/ns dual-pulse LIBS analytic survey for copper-based alloys. Appl. Surf. Sci. 254 (2007) 863-867.

[34] D. Scuderi, O. Albert, D. Moreau, P. P. Pronko, and J. Etchepare, Interaction of a laser-produced plume with a second time delayed femtosecond pulse, Appl. Phys. Lett. 86 (2005) 071502.

[35] J. Hermann, S. Noël, T. E. Itina, E. Axente and M. E. Povarnitsyn, Correlation between ablation efficiency and nanoparticle generation during the short-pulse laser ablation of metals , Laser Physics 2008, Vol. 18, 374-379.

[36] Y. Lu, V. Zorba, X. Mao, R. Zheng and R.E. Russo, UV fs/ns Double-Pulse Laser Induced Breakdown Spectroscopy for High Spatial Resolution Chemical Analysis,J. Anal. At. Spectrom. 2013, 28, 743-748.

[37] D. R. Lide, CRC Handbook of Chemistry and Physics (CRC Press, Boca Raton, 1994).

[38] National Institute of standards and technology, Atomic spectra database. (http://physics.nist.gov/PhysRefData/ASD) and KURUCZ atomic spectral line database (http://www.pmp.uni-hannover.de/cgi-bin/ssi/test/kurucz/sekur.html)